Understanding the pyrolysis-assisted conversion of metal salt-impregnated biomass into biogas and nanocatalyst-coated porous biochar

Mengqi Tang[a,*], Alexandre Chevillot-Biraud[a], Stéphanie Lau-Truong[a], Ahmed M. Khalil[b], Mohamed M. Chehimi[a,*]

[a]Université Paris Cité, CNRS, ITODYS (UMR 7086), Paris, 75013, France
[b]Photochemistry Department, National Research Centre, Dokki, Giza, 12622, Egypt.

[*]Corresponding author.
E-*mail address:* mohamed.chehimi@cnrs.fr (M. Chehimi)
   mengqi.tang@etu.u-paris.fr (M. Tang)

Abstract

Slow pyrolysis is the most employed technique to design biochar at high yield. It is particularly suitable for converting impregnated biomass into biochar-immobilized nanocatalysts. The latter exhibits a porous structure compared to pristine biochar. However, this distinct behavior is yet to be understood. To this end, the coupled technique of Thermogravimetric Analysis/Fourier Transform Infrared Spectroscopy (TGA/FTIR) was used to simulate pyrolysis in a tube furnace for biochar production and to analyze syngas. Sugarcane bagasse (SCPB) powder, treated with copper and/or nickel nitrates, was pyrolyzed in a TGA under nitrogen at heating rates from RT to 500 °C for 1 hour. TGA/DTG permitted monitoring the thermal events of SCPB which was found to be exacerbated by the introduction of metals. The syngases, including CO_x, NO_x, HNO_3, and H_2O, were effectively detected and analyzed by FTIR during the pyrolysis process at varying heating rates of 10, 20, and 30 °C/min. Notably, $Ni(NO_3)_2.6H_2O$ yielded N_2O, probably associated with the formation of a biochar porous structure. The pyrolysis activation energies (E_a) of SCPB and SCPB/CuNi were determined using FWO and DAEM models. The maximum weight loss was found to occur at a thermochemical conversion of ~60% into char; and Ea = 234 kJ.mol^{-1} for SCPB, much higher than 90 kJ.mol^{-1} obtained for the wet impregnated sample SCPB/nitrates; hence the dramatic effect of the nanometal precursors on the pyrolysis process. XPS analysis demonstrated that TG-biochar and "tubular furnace" biochar exhibit identical surface chemical compositions. Raman spectroscopy brought evidence for graphitic carbon structure as judged from D and G bands in SCPB/CuNi. Microscopic observations confirmed a well-defined porous morphology.

From the above, this TG-FTIR study permitted to highlight the central role of copper and particularly nickel in the pyrolysis process. These metals:

-significantly lower the pyrolysis activation energy
- induce porous structure of the underlying biochar
-could be added to the repertoire of activators, dominated by $ZnCl_2$ and $FeCl_3$.
-serve as activators

Keywords: thermochemical conversion; biochar; *Saccharum officinarum*; wet impregnation; pyrolysis activation energy.

Graphical abstract

3
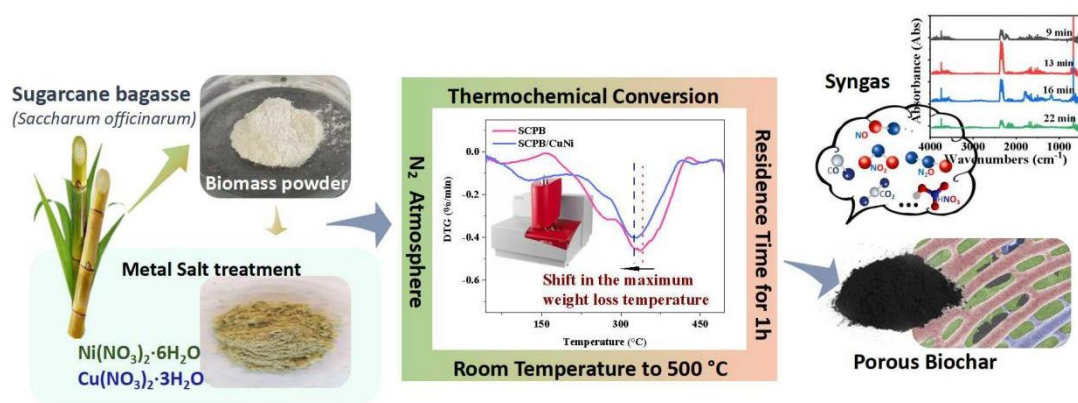
Introduction

The 2030 Agenda for Sustainable Development provides a shared blueprint for peace and prosperity for people and the planet[1,2]. Amid growing concerns over energy and environmental challenges, the development of emerging materials and clean fuels has been recognized as major contributors to environmental remediation[3,4]. In recent years, biomass has emerged as a promising, sustainable, and environmentally friendly precursor[5]. Agricultural waste is one of the abundant yet underutilized resource of biomass[6]. Certain types of agricultural byproducts, such as peapod peel[7], corn straw[8], and sugarcane pulp bagasse[9], are rich in cellulose, and their high yield and carbon content make them suitable feedstocks for renewable energy production. Converting biomass energy into valuable products is an effective and sustainable way to address the problems of energy shortage and waste abundance[10].

Pyrolysis, a thermochemical process conducted under specific conditions, is widely used to transform biomass into various valuable products. Depending on the heating rate, biomass pyrolysis can be categorized into slow pyrolysis (primarily yielding gas or char) and fast pyrolysis (aimed at producing bio-oil) [11-13]. Among the pyrolysis products, biochar has garnered significant attention, involving heating biomass to moderate temperatures in an oxygen-free or low-oxygen environment[14]. Biochar is a sustainable carbon-rich solid material of interest in energy storage[15] and environmental remediation[16,17]. Over the recent years, it emerged as remarkable, renewable support of nanocatalysts, and an excellent alternative to the classical supports silica, alumina, and zeolite[18,19]. The composition of biochar derived from biomass thermochemical conversion mainly depends on the initial composition of the feedstock in cellulose-, lignin-, hemicellulose-, protein- and chitin [20].

The addition of mono- and bimetallic catalysts during synthesis has been shown to enhance pyrolysis efficiency and product quality (*e.g.*, biochar yield, porous structure) [21,22], with examples including Mg [23], Cu[24], Co-Ni[25], Mn/Co[26], and Mg/Fe [27]. Towards this end, wet impregnation of the raw biomass with catalyst precursors is an efficient and simple method of creating metal-loaded biochar composites by pyrolysis [28,29]. This approach enhances the dispersion on- and bonding of the

4

nanometals to the biochar matrix and promote the formation of porous structures during the subsequent carbonization process[30].

Another noteworthy aspect, syngas, kind of simultaneous product of biomass thermochemical conversion, can be effectively detected and collected, which might be another benefit for gaseous fuel and reaction atmosphere [31,32]. In this regard, commonly used model-free methods for the decomposition mechanisms and kinetics of lignocellulosic biomass pyrolysis, are highly effective for determining the activation energies [33,34].

To elucidate the relationship between the syngas generated and the formation of porous biochar structure, thermogravimetric analysis coupled with Fourier Transform Infrared Spectroscopy (TGA-FTIR) was employed to simulate the pyrolysis process. While TGA provides insights into the decomposition and weight loss of biomass as a function of temperature, FT-IR enables continuous analysis of gases released during the process[35]. Monitoring the weight loss versus time and temperature permits to determination of pyrolysis activation energy using appropriate kinetic models [36].

This study aims to analyze the pyrolysis of SCPB biomass impregnated with metallic salts, and to understand the development of porous biochar-metal composites at different pyrolytic parameters; and detect the generation of syngas during the thermo-chemical transformation. Specifically, a series of experiments were conducted to

(1) Examine the development of pore structure of biochar with different amounts of metal nanoparticles (Cu, Ni, and CuNi) and different heating rates (10, 20, and 30 °C/min);

(2) Explore the composition of the released syngas in this process.

(3) Reveal the thermal transformation process using a kinetic model, activation energy calculation, and elemental analysis.

Despite the publication of several articles on the TGA study of the thermochemical conversion of biomass into biochar, to the best of our knowledge, such an investigation has never concerned biomass impregnated with copper and/or nickel salts. For this

5

reason, we were motivated to employ TGA to understand the formation of porous biochar-supported nanocatalysts [37,38] by the direct pyrolysis of biomass impregnated with metal nanocatalyst precursors. Not only these salts provide immobilized nanocatalysts but also induce the formation of a remarkable fishnet porous structure of the underlying biochar.

2. Materials and methods

2.1. Sample preparation

The sugarcane pulp bagasse (SCPB) utilized in this study was collected from Eygpt. The SCPB was crushed and then milled to fine powder for pyrolysis experiments. Copper nitrate, nickel nitrate and their mixture were employed respectively to wet impregnation process in distilled water, the mass ratio sets in 0.5 mmol of metal nitrate per gram of biomass, which named SCPB/Cu, SCPB/Ni and SCPB/CuNi.

2.2. TGA-FTIR of SCPB-based samples

A Setaram Labsysevo apparatus was used under nitrogen atmosphere, and coupled with Fourier Transform Infrared Spectroscopy (Thermoscientific Is 10) to detect gaseous products.

The blank experiments were performed before each test to ensure accuracy. SCPB-based samples were exposed to constant temperatures over time and N_2 ensured inert conditions before testing. The furnace temperature was raised to the target pyrolysis temperature from RT to 500 °C. The heating rate was set between 10 and 30 °C/min, and the final temperature was maintained for 1 h. After cooling to RT at the end of the experiment, biochar samples were collected for further analysis.

For each test, the TG curve (mass loss curve) and the derivative mass loss curve (DTG) were monitored and calculated as the indicator of the mass loss ratio and the endothermicity, as defined by Eq. 1 and Eq. 2, respectively.

$$Mass\ residence\ ratio\ \% = \frac{M_T}{M_0} \times 100 \qquad (1)$$

$$DTG = \frac{d(TG)}{d(T)} \tag{2}$$

M_0 and M_T represent the initial mass and the residual mass of the sample at temperature T[36].

2.3. Kinetics modeling

The Flynn-Wall-Ozawa (FWO) method and the distributed activation energy model (DAEM) were applied for fitting pyrolysis kinetics and determining the pyrolysis activation energy (E_a) at different conversion rates [34,39,40]. These methods are the most employed due to their reliability.

The FWO and DAEM methods are expressed by the following Eq. (3-4):

$$\ln(\beta) = \ln(\frac{AR}{E_a}) + 0.6075 - \frac{E_a}{RT} \tag{3}$$

$$\ln(\frac{\beta}{T^2}) = \ln\left[\frac{AE_a}{Rg(\alpha)}\right] - 5.531 - 1.052\frac{E_a}{RT} \tag{4}$$

The degree of conversion rates α was calculated using the following Eq. (5):

$$\alpha = \frac{w_0 - w_t}{w_0 - w_f} \tag{5}$$

where w_0, w_f and w_t are the mass of the sample at the initial, final, and time t stages, respectively (mg). β is the heating rate (K/min), R is the universal gas constant (8.315 J/mol·K), T is the absolute temperature in Kelvin (K), A is the pre-exponential factor (min^{-1}), and E is the activation energy (kJ/mol).

The corresponding activation energy E_a was obtained from the slope of the line plotted by $\ln(\beta)$ and $\ln(\beta/T^2)$ versus 1/T in the conversion rate α. This linear fitting approach allows for accurate activation energy calculation, at different stages of the pyrolysis process, reflecting how the energy requirements change as the reaction progresses.

2.4. Characterization of the biochar products

X-ray photoelectron spectroscopy (XPS) analyses were performed using a K Alpha+

7

apparatus (Thermo, East Grinstead, UK), fitted with a mono Al Kα (source energy = 1486.6 eV) and a flood gun for charge compensation. Avantage software version 6.8.0 was used for data acquisition and processing. The pass energy was set at 80 and 200 eV for the narrow regions, and the survey spectra, respectively. The surface chemical composition was determined using the manufacturer's sensitivity factors.

Raman spectra of the samples were acquired using a Horiba HR Evo Nano, a high-resolution Raman microspectrometer. The excitation source was a 473 nm laser. The laser was focused onto the samples using a 100x long-distance objective (N.A. = 0.9), which allows for high spatial resolution when the experiments were performed in air. The spectrometer was coupled to the microscope, enabling precise localization of the measurement points to ensure high signal-to-noise ratios for reliable analysis.

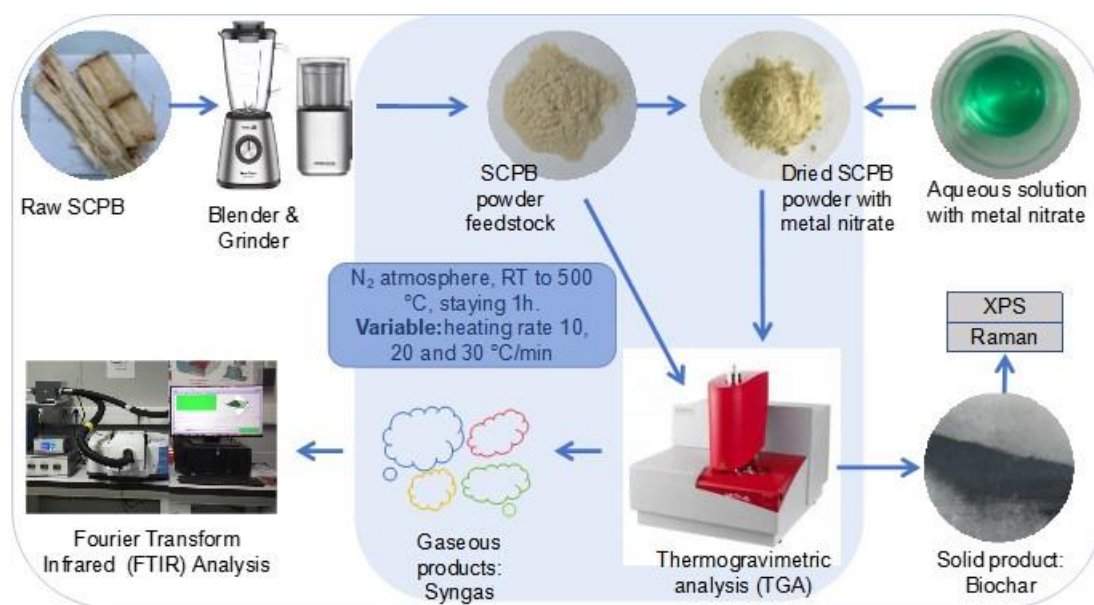## 3. Results and Discussion

3.1. Workflow

Fig. 1. Workflow scheme of the Pyrolysis Process of SCPB-based biomass.

The biomass decomposition and the gaseous products during thermochemical conversion were studied using TG-FTIR simulated tubular furnace pyrolysis. Based on

8

our previous research on SCPB biomass as the feedstock, catalyst precursors (copper nitrate and nickel nitrate) were loaded onto the biomass using the wet impregnation method[37]. During the subsequent pyrolysis process, the pyrolysis temperature of 500 °C was found to be optimal for catalytic activity and energy efficiency[41]. For analyzing the thermal degradation of SCPB residues, both with and without catalyst precursors, the heating ramp rate was set to 10, 20, and 30 °C/min, and the generated biochar as the solid product was probed ex-situ by XPS and Raman spectroscopy, whereas the syngas were collected during pyrolysis and analyzed in-situ by the FTIR detector.

3.2. TGA/DTG study

Table 1. Thermal decomposition characteristics of SCPB and CuNi

Sample	Decomposition Stage	Temperature Range (°C)	Key Observations
SCPB	Water	~150	WL ~5 wt%; Water molecule evaporation.
	Hemicellulose	156–267	WL ~14 wt%; Amorphous structure and lower thermal stability.
	Cellulose	267–421	WL ~50 wt%; Formation of volatiles; significant mass loss.
	Lignin	200–500	Gradual breakdown over a broad range
	Residual stage	500 (1h hold)	~23 % residual mass remained unchanged.
CuNi	Crystalline water	<156	WL ~5 wt%; Water release.
	Nitrate groups	156–221	WL~12%; Loss of nitrate groups as gas.
	Conversion of metal ions	227–364	WL~33%; Formation of metal oxides.
	Residual stage	500 (1h hold)	~45% residual mass remained unchanged.

wl refers to weight loss

The thermal decomposition behaviors of SCPB, CuNi, and SCPB/CuNi composites revealed distinct characteristics shown in Table 1 and Fig. 2. SCPB exhibited multi-stage decomposition, with water evaporation, hemicellulose degradation, cellulose breakdown, and gradual lignin decomposition contributing to biochar formation[42]. CuNi underwent three stages: crystalline water release, nitrate decomposition to HNO_3[43], and conversion of metal ions to oxides[43], leaving a stable residual mass.
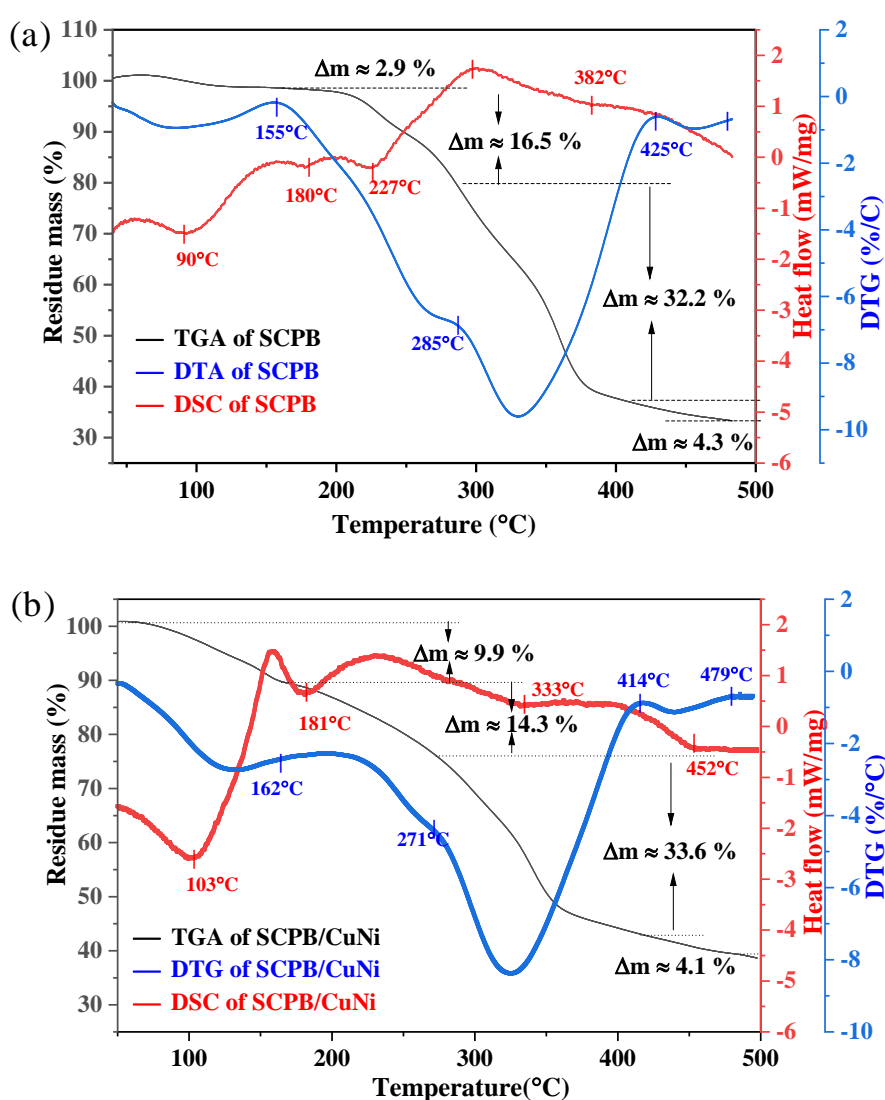

Fig. 2. The TG/DTG/DSC curves vs pyrolysis temperature of SCPB(a) and SCPB/CuNi(b).

In Fig. 2a, the TGA/DTG/DSC curves show the characteristic thermal degradation of SCPB. Initially, SCPB experiences a mass loss of 2.9% at 155 °C, which is attributed to the volatilization of the organic content. Subsequently, about 17.5% of the mass is lost at 285 °C due to the degradation of unstable organic components, such as hemicellulose and carbohydrates[44]. At 336 °C, the initial mass of the biochar is further lost by 32.2%, which is mainly due to the degradation of cellulose[45]. Beyond 425 °C, the decomposition of refractory organic carbon (mainly lignin) occurs. In the presence of metal salts copper nitrate and nickel nitrate, the degradation of biochar occurred uniformly between 150 and 480 °C (Figure 2b), the pyrolysis plot of SCPB/CuNi is more similar to that of pure SCPB. This suggests that, while the addition of CuNi did not change the overall behavior significantly, it did affect the maximum mass loss rate, as shown in the corresponding DTG derivative (Fig. S1): SCPB/CuNi composite peaks at 328 °C, which is 10 °C lower than pure SCPB (338 °C) and 5 °C higher than CuNi (323 °C). Compared with the pure SCPB, the DTG curve of SCPB/CuNi showed that CuNi reduced the degradation temperature of biomass, while improving the degradation rate and gas release to form special products.

Heat flow analysis of SCPB precursor and SCPB treated with metal salts showed that there was an interaction between metals and biochar (Fig. 2a-b red line). The endothermic peak of biochar (180 °C) was retained by SCPB/CuNi, while some of the peaks also changed. The presence of these thermal events and the exo/endothermic drift may support the existence of electrostatic or metal exchange interactions between metal ions and functional groups on the surface of biochar[44].
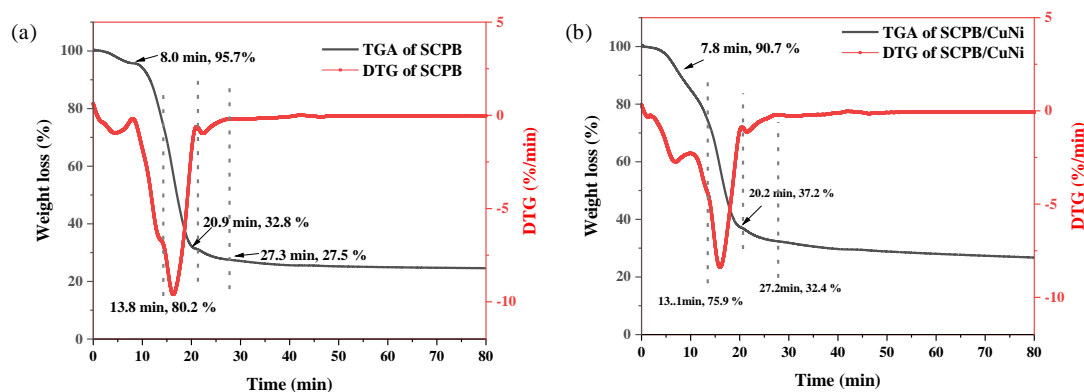

Fig. 3. TG/DTG curve vs pyrolysis time of SCPB(a) and SCPB/CuNi(b).

From the TG/DTG curves vs pyrolysis time in Fig.3, which can be seen that the mass of the pure biochar SCPBB and biochar composite SCPBB/CuNi remain stable after 1h at 500 °C under TG pyrolysis, with a residual content of ~24% and ~27%, respectively. To further evaluate the interactions between CuNi and SCPB during the thermal reaction, the theoretical mass loss of the blend (SCPB/CuNi-t) was calculated as the weighted average of the individual mass losses of CuNi and SCPB. This approach assumed no synergistic effects between the two components. The theoretical mass loss is expressed according to Eq.(6) [46]:

$$W_{SCPB/CuNi-t} = R_{CuNi} \times W_{CuNi} + R_{SCPB} \times W_{SCPB} \tag{6}$$

R_{CuNi} and R_{SCPB} are the weight rates of CuNi and SCPB in the SCPB/CuNi composite. W_{CuNi} and W_{SCPB} represent the weight mass loss of pure CuNi and SCPB, respectively.
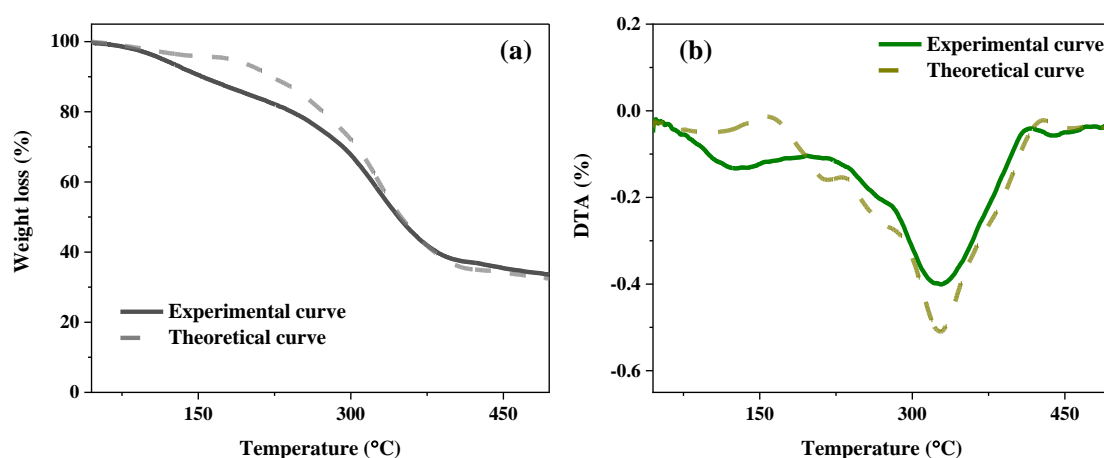

Fig. 4. Experimental and theoretical TGA curves (a), and DTG plots (b) of SCPB/CuNi composite.

Fig.4 illustrates a TG/DTG comparison between the theoretical mass loss and the actual experimental one of the SCPB/CuNi composite. The deviations from the theoretical values confirmed the presence of synergistic interactions between SCPB and CuNi during the thermal behavior. Therefore, it is noteworthy that loading metal ions into SCPB biomass material dramatically affected the pyrolysis of the latter, resulting in the formation of a porous structure for the biochar/metal composites.

12

3.3. Analysis of the released gases

The product distribution of SCPB-based materials during pyrolysis under N_2 atmosphere has been investigated by a hyphenated platform TG-FTIR, revealing their interactions between the components. As shown in Fig. 5, the plane and 3D infrared spectra respectively exhibit the absorption peaks of SCPB, SCPB/Cu, SCPB/Ni, and SCPB/CuNi.

All of SCPB-based samples showed strong infrared absorption between 7-22 min, corresponding to a temperature range of 140–450 °C. The maximum infrared absorption of SCPB and SCPB/CuNi occurred at 16 min, corresponding precisely with the peak of the maximum weight loss rate displayed in DTG curves. It was observed that the maximum infrared absorption of SCPB/CuNi at slightly lower temperatures, suggesting that the addition of metal nitrate promoted the co-pyrolysis process with biomass precursor.

The FTIR analysis identified the major functional groups, the stretching vibration bands around 1650-1850 cm^{-1} were attributed to N-O[47,48], while the bands between 1000-1450 cm^{-1} corresponded to C-H and C-O bonds[46,49]. Additionally, several pyrolysis products were identified based on their characteristic IR bands, including CO_2 (2400-2240 cm^{-1}), CO (2240-1980 cm^{-1}), CH_4 (3200-2850 cm^{-1}), and H_2O (3500-4000 cm^{-1}), which was a typical feature of the reported pyrolysis process of the lignocellulosic biomass [49-51]. During the initial heating phase, the FTIR spectra of hydrated nitrates exhibited broad peaks corresponding to O-H groups and lattice water at approximately 400 cm^{-1} and 1630 cm^{-1}, respectively.

Upon loading Ni nitrate onto SCPB in Fig.5c-d, the 3D infrared spectra of SCPB/CuNi exhibited a distinct gas release around 7 minutes, similar to SCPB/Ni, along with a band at ~ 2200 cm^{-1} attributed to N_2O [52]. This behavior is absent in the single SCPB and SCPB/Cu(Fig.5a-b), implying that the presence of nickel nitrate with the pyrolysis parameter facilitated this gas evolution.
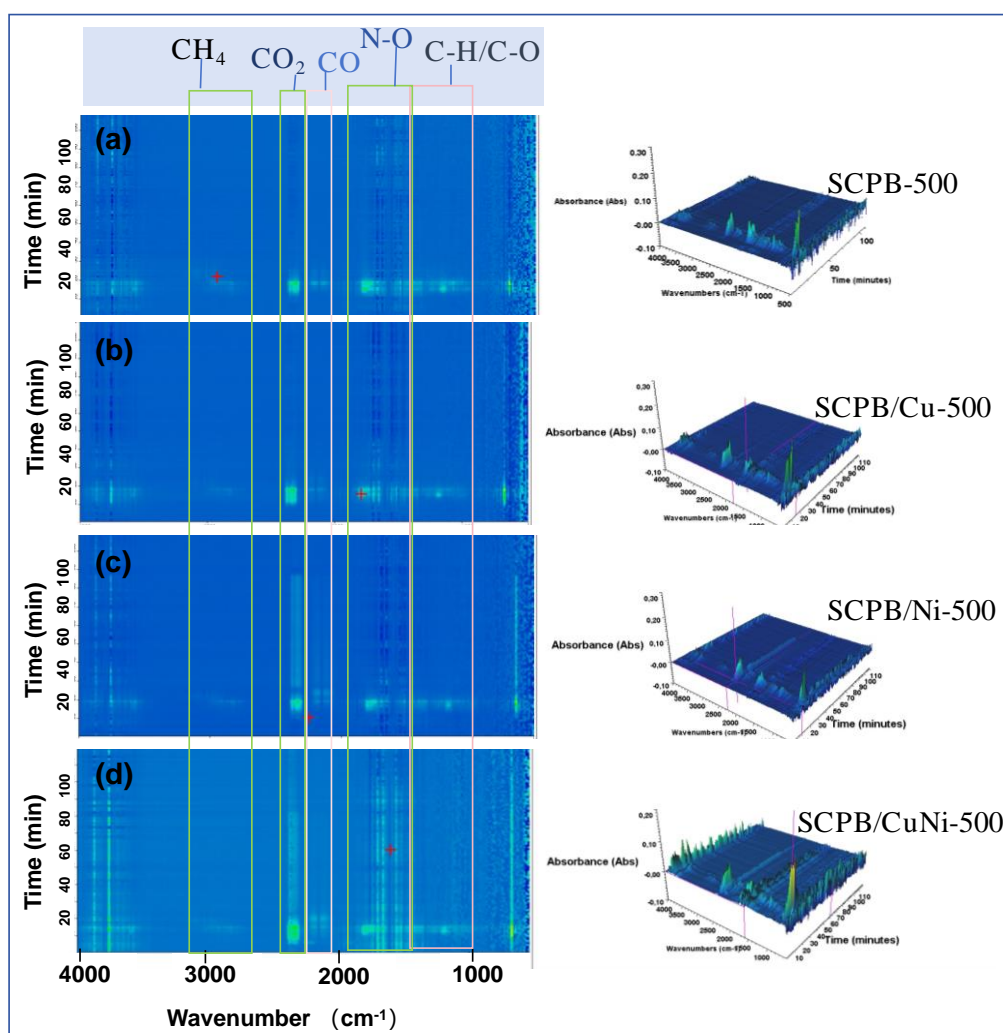
13

Fig. 5. 3D FT-IR spectra of products during pyrolysis at 500°C and heating rate of 20°C/min: (a) SCPB, (b) SCPB/Cu, (c) SCPB/Ni, and (d) SCPB/CuNi.

Furthermore, comparing different heating rates of thermal conversion, the composition of the evolved mixed gases was investigated for biomass precursor SCPB, catalyst CuNi and their composite SCPB/CuNi at different heating rate, extracted 2D spectra during 110-360°C. Figure 6a-c shows that the spectrum of the gases evolved at 10 min indicates that the quantity of CO_x, N_xO_x, O_3 and HNO_3 [47,48,53] generated increases generally with the increase of heating rate from 10 °C to 30 °C, thus emphasizing that the heating rate is a key factor of thermal treatment in controlling gas yields during the process. The spectra of all samples presented similar peaks within same temperature ranges. Figure 6d revealed the weight residual mass profiles reveal that biochar yields remained remarkably consistent (± 1.5%) across heating rates of 10–30°C/min.
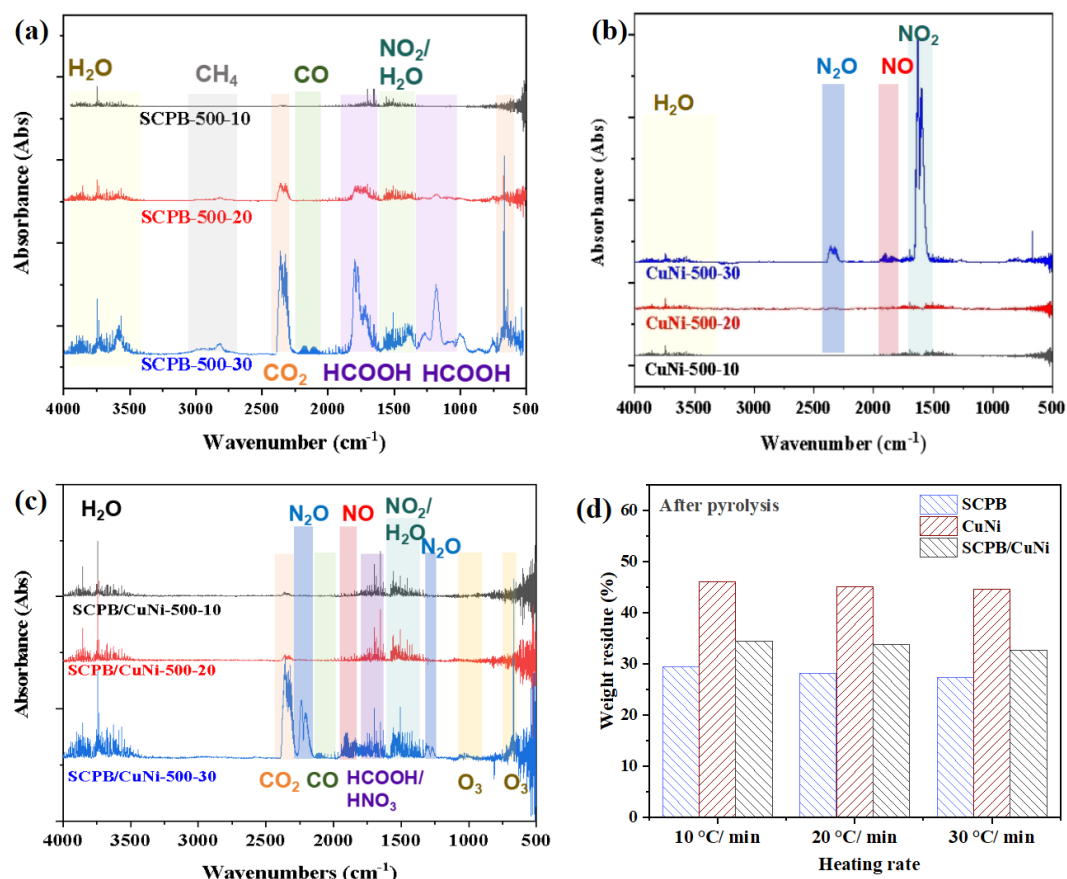
14

Fig. 6. FT-IR spectra of SCPB(a), CuNi(b), SCPB/CuNi(c) during pyrolysis with different heating rate of 10, 20 and 30°C/min. The spectra were taken at 10 min. The weight residue of samples after pyrolysis treatment(d).

3.4. Kinetics analysis

Model-free methods calculated overall kinetic parameters to the decomposition process for pyrolysis conversion, requiring no assumptions about the reaction mechanism[54]. The TG data of SCPB and SCPB/CuNi at different heating rates (10, 20, and 30°C/min) were analyzed using 2 kinetic model methods, included Flynn-Wall-Ozawa (FWO, Fig. 7) method and Distributed Activation Energy Model (DAEM, Fig. S2) with the conversion rates (α=0.1-0.9) [12].
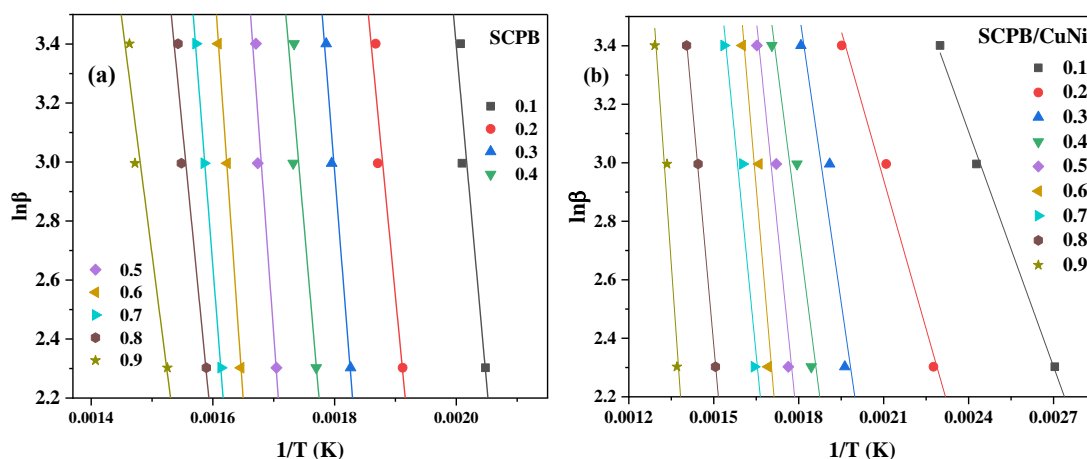
15

Fig. 7. Kinetic plots of SCPB(a) and SCPB/CuNi(b) according to FWO methods.

By calculating the conversion rates, using the relationship between the heating rate function and the inverse of temperature plotted followed by linear fitting. Both methods provided good linear fitting results, and as α increased, the fitting curves became increasingly parallel, leading to more accurate and reliable estimates of the activation energy (Ea) by the slope, as shown in Table 2.

Ea corresponds to reaction rates and kinetic stability[55]. It was significantly observed that the Ea of SCPB/CuNi is significantly lower than that of SCPB at different conversion rates, indicating that the pyrolysis reaction for SCPB/CuNi was easier to proceed. Therefore, the introduction of metal nitrate with impregnation treatment, as a pyrolysis catalyst, enhanced the catalytic activity and reduced the required energy for the reaction of pure biomass SCPB.

Table 2. Activation energy E_a of SCPB and SCPB/CuNi at different conversion rates.

Conversion rate	SCPB			SCPB/CuNi		
	Slope	Intercept	E_a /kJ·mol^{-1}	Slope	Intercept	E_a /kJ·mol^{-1}
0.1	-22915.3	49.22	181.11	-2678.46	9.53	22.27
0.2	-21433.32	43.27	169.4	-3397.32	10.08	26.85
0.3	-26067.54	49.89	206.03	-6677.76	15.54	52.78
0.4	-23803.17	44.44	188.13	-7521.13	16.30	59.44
0.5	-28455.54	50.79	224.9	-9524.26	19.21	75.28
0.6	-29611.13	51.05	234.03	-11371.38	21.68	89.87
0.7	-26370.27	44.84	208.42	-9876.28	18.64	78.06
0.8	-21036.56	35.72	166.26	-10813.17	18.60	85.46

16

| 0.9 | -16012.82 | 26.71 | 126.56 | -13833.40 | 21.33 | 109.33 |

3.4. Characterization of the solid products obtained by TG-FTIR.

Following the TG-FTIR investigations, the solid samples were recovered from the crucibles and examined by XPS and Raman spectroscopy to account for the formation of metal-loaded biochar during thermal analysis.

3.4.1. Surface chemical analysis by XPS

XPS was used to monitor the change in the surface chemical composition of the biomass upon wet-impregnation and thermal analysis in TGA under nitrogen. The survey spectra are shown in Figure 8a for the biomass and the resulting chars loaded with mono and bimetallic systems. The main peaks are C1s (285 eV), O1s (532 eV), N1s (400 eV), Cu2p (930-965 eV), and Ni2p (850-884 eV). Single metal systems show the respective elements; the Cu2p and Ni2p spectra co-exist for the pyrolyzed biomass loaded with copper and nickel nitrates. Thermal treatment leads to carbon-richer matter, hence the lower O1/C1s intensity ratio noted for the chars compared to the initial biomass. Drastic change occurs in the case of C1s ; the lignocellulosic matter has typical C1s spectrum [56], exhibiting sp^3 carbon atoms in C-C/C-H bonds at 285 eV followed by C-O component at ~286.2 eV and acetal group O-C-O characteristic of cellulose of which component is centered at 288.0 eV (Fig.8b). The thermal analysis under nitrogen yields char which has a typical skewed high-resolution C1s spectrum typical of carbon materials. The main peak is centered at 284.2 eV, with lower binding energy consistent with sp² carbon atoms (Fig.8c). Figure 8d shows a peak-fitted N1s spectrum from sugarcane bagasse, an amine-type nitrogen with a small portion from a quaternized nitrogen (hydrogen bonds or protonation); SCB is known to contain less than 1% nitrogen [57]. Upon thermal treatment, rearrangements of the functional groups yield three major nitrogen-containing groups in biochar: pyridinic, pyrrolic, and graphitic nitrogen atoms giving rise to a more complex N1s peak structure (Fig.8e) which is fitted with three components centered at ~398.2, 399.9 and 401.4 eV,
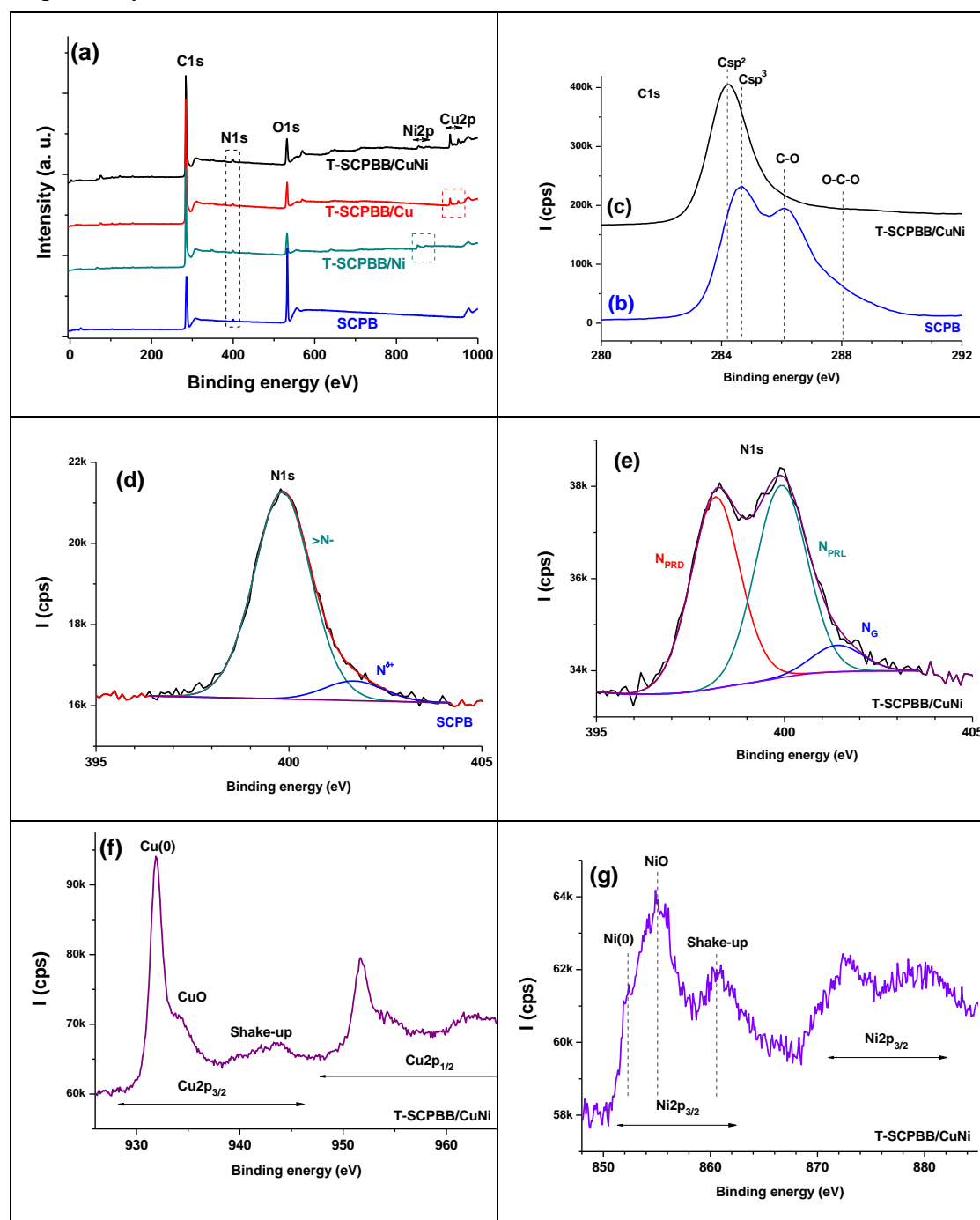
17

respectively.

Fig. 8. XP spectra of the biomass and resulting biochar-loaded nanocatalysts : (a) survey regions, (b) and (c) high-resolution C1s spectra, (d) peak-fitted N1s from the biomass, (e) peak-fitted N1s from T-SCPBB/CuNi, (f) and (g) high-resolution Cu2p and Ni2p spectra of T-SCPBB/CuNi, respectively.

As per the transition metals, the pyrolysis of wet-impregnated biomass under nitrogen flow yields bimetallic nanoparticles with alloyed copper and nickel [58], or single metallic systems (pure copper or pure nickel). For the bimetallic system, Cu2p and Ni2p

18

are displayed in Fig. 8f and 8g, respectively. Cu2p is dominated by metallic copper component at 932.0 eV but with some extent of CuO, as judged from the component at 934.1 eV and particularly its shake-up satellite (Fig.8f), characteristic of oxidation state (II). The nickel is oxidized, yet it shows substantial fraction of metallic nickel of which $Ni2p_{3/2}$ peak is centred at 852.3 eV (Fig.7g).

Table 3 reports the surface chemical composition of the biomass and the chars. The compositions of the « TGA chars » are compared to those we reported for the « Tubular furnace chars ».

Table 3. Surface chemical composition of the pristine biomass, « TGA chars », and biochars obtained by pyrolysis.

Materials	N/C	O/C	(Cu+Ni)/C
SCPB (biomass)	0.019	0.414	-
T-SCPBB/Cu	0.017	0.122	0.0065
SCPBB/Cu	0.014	0.199	0.0070
T-SCPBB/Ni	0.018	0.138	0.0093
SCPBB/Ni	0.015	0.189	0.0056
T-SCPBB/CuNi	0.021	0.157	0.0245
SCPBB/CuNi	0.0168	0.194	0.0118

The N/C atomic ratio surprisingly remains the same although the thermal treatment yields a carbon-rich material. This supports the formation of nitrogen-doped carbon by thermal treatment. In contrast, O/C significantly decreases by nearly three-fold.

3.4.2. Raman spectra

The Raman spectroscopy revealed distinct peaks corresponding to the major components, coupled with Raman microscopy demonstrated the image of the morphological surface. Raman spectrum has been reported for qualitative analysis of the cellulose and lignin[59]. Lignin is an aromatic polymer whose associated band does not overlap with the carbohydrate bands, the peak position serves as a reliable marker for lignin presence[60]. However, hemicellulose and cellulose share similar functional groups and chemical bonds, resulting in the overlapping of the associated bands in the Raman spectrum[59,61].

For the SCPB sample in Fig. 9a , the peaks at 1264 cm^{-1}, 1605 cm^{-1} and 1631 cm^{-1}

19

corresponded to lignin, the peaks at 1092 cm^{-1} and 1170 cm^{-1} are associated with cellulose rich in SCPB, which were visible in the Raman spectrum[62]. After the raw SCPB was treated with wet impregnation to obtain SCPB/CuNi sample (Fig. 9b), the peak positions of its lignocellulose structure showed almost no change just a slight reduction of intensities. Furthermore, the characteristic peaks of metal nitrites at 1326 cm^{-1} and 980 cm^{-1} associated with nitrate and nitrite[63,64], two bands at 336 cm^{-1} and 587 cm^{-1} were ascribed to Cu-O and Ni-O[65]. It could be due to nitrate ions attached to the biomass support and metal ions bound to the functional groups of biomass, These peaks appeared together with the cellulose and lignin peaks to suggest the metal nitrates have been successfully introduced by the wetness impregnation method.

Nevertheless, during the pyrolysis process, another critical transformation that needed attention was when both lignin and cellulose were decomposed and their characteristic peaks completely disappeared in Fig. 9c, with new peaks appearing, and assigned to the SCPBB biochar-based sample instead. The two distinct peaks observed at 1359 cm^{-1} and 1589 cm^{-1} correspond to the D band and G band, respectively. The D band represents defects of carbonaceous material, while the G band indicates the presence of an ordered graphitic structure, confirming the fabrication of biochar material. Fig.9d shows the positions of the metal oxides in SCPBB/CuNi shifted slightly after pyrolysis, which potentially was attributed to the formation of CuNi [66].

Another important aspect was Raman imaging, the surface structure of the untreated SCPB sample (as shown in Fig.8a) appears a dense fibrous appearance[67]. After the wet impregnation treatment, the metal nanoparticle loaded on the SCPB sample still retained its fiber structure without significant disruption (Fig.8b). As shown in Fig. 8c and d, it is evident that the pyrolysis process leads to the decomposition of lignin and cellulose, resulting in a significant transformation into a carbonaceous structure. Notably, the biochar composition SCPBB/CuNi exhibits a unique porous structure with an ordered arrangement due to the loading of metal nanoparticles, consistent with previously reported SEM images[68]. This porosity was closely related to the gas products detected in the TGA/FT-IR analysis mentioned earlier, indicating a significant

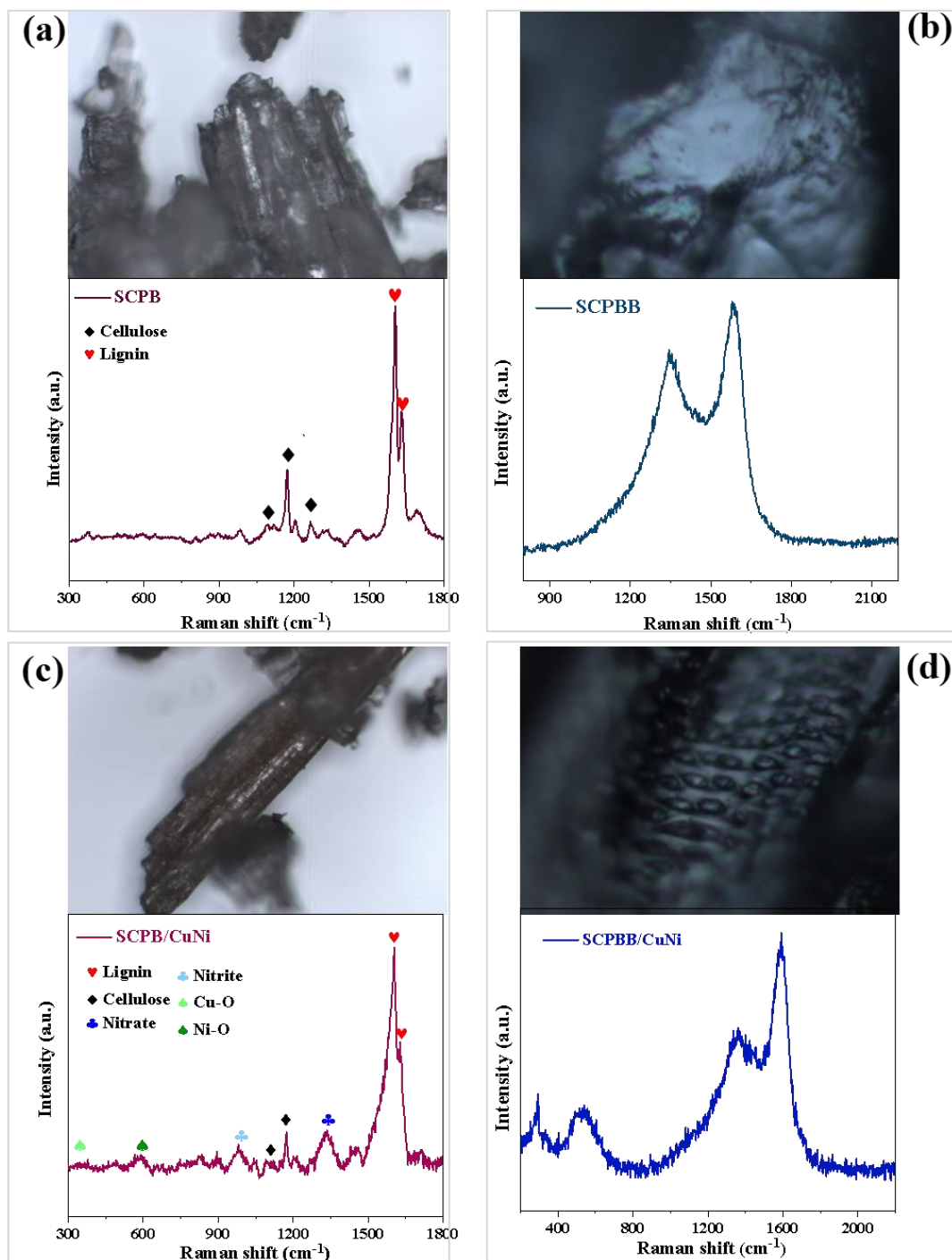connection between the structural changes and the release of gases during pyrolysis.

Fig. 9. Raman spectra and corresponding magnified morphology images of biomass precursors：SCPB(a)，SCPB/Cu&Ni nitrates (b) and their biochar products SCPBB (c)，SCPBB/CuNi (d).

3.5. Proposed mechanisms of porous biochar@nanometal formation

Through examining the characteristics of the generated gases and the change in the solid products, previous experimental references, a preliminary understanding of the reaction mechanisms was developed, attempting to elucidate the reaction pathways of different components during the pyrolysis process. This process involves the pyrolysis of metal-ammonia complexes ($Cu(NH_3)_2·3H_2O$ and $Ni(NH_3)_2·6H_2O$) along with biomass ($C_xH_xO_x$) in a nitrogen atmosphere, heating from room temperature (RT) to 500°C. The steps are summarized below in Fig.10 :
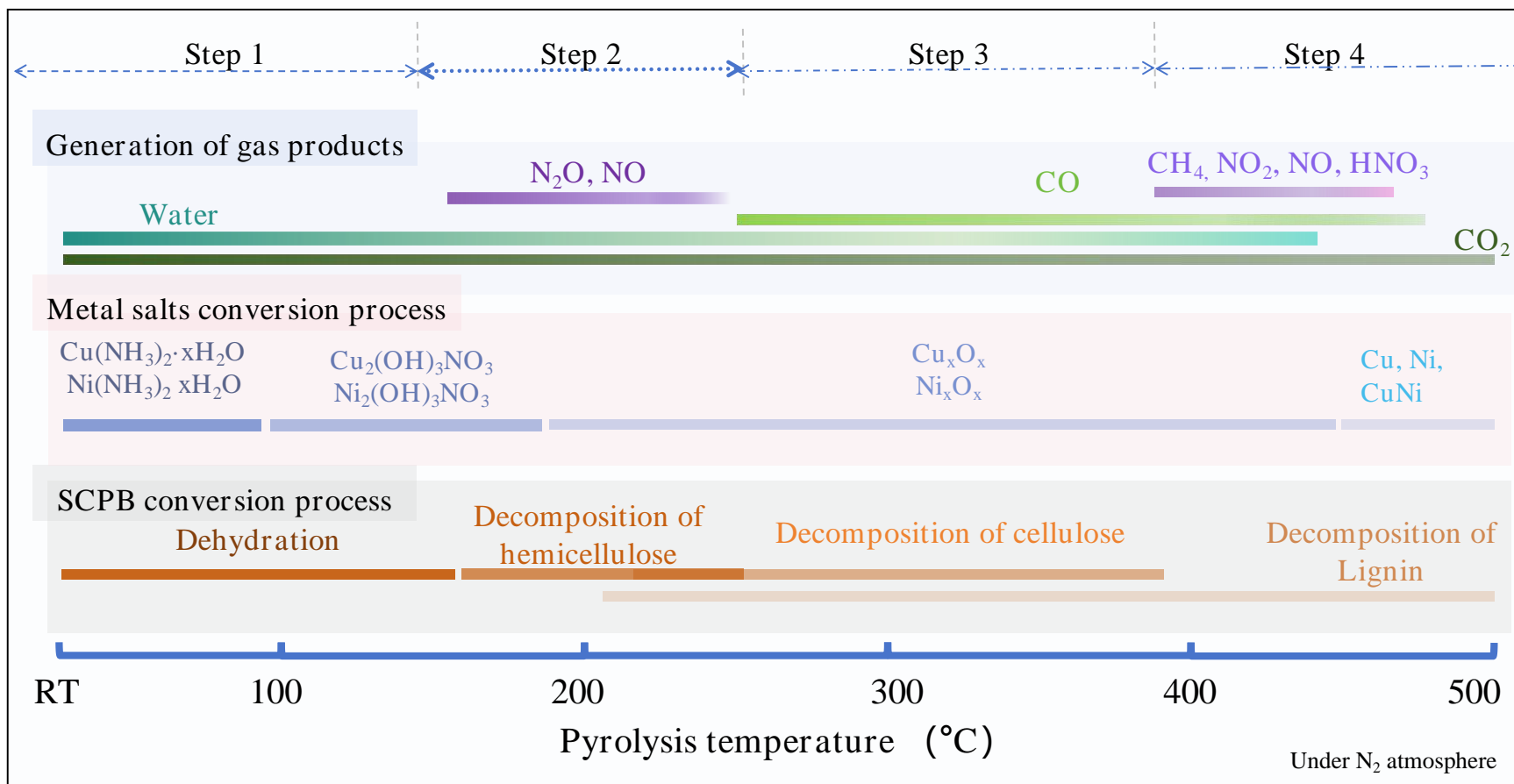
Fig. 10. Degradation profile of solid and gaseous phases during the pyrolysis process.

Step 1: Dehydration and Decomposition (50–170 °C)

The metal salts $(Cu(NH_3)_2 \cdot nH_2O$ and $Ni(NH_3)_2 \cdot nH_2O)$ and biomass $SCPB(C_xH_xO_x)$ undergo dehydration as the temperature increases, losing water molecules.

This results in the formation of metal hydroxides in the presence of heat, such as $Cu_2(OH)_3NO_3$ and $Ni_2(OH)_3NO_3$, along with water vapor [69,70].

Key Reactions:

$$M(NH_3)_2 \cdot nH_2O + SCPB(C_xH_xO_x) \rightarrow M_2(OH)_3NO_3 + SCPB(C_xH_xO_x) + xH_2O$$

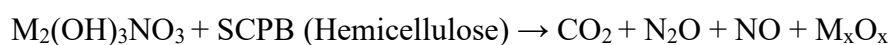(Where M = Cu or Ni)

Step 2: Reaction with Biomass (170–280 °C)

The metal hydroxides (like $Cu_2(OH)_3NO_3$ and $Ni_2(OH)_3NO_3$) react with biomass components, particularly hemicellulose (SCPB), leading to the release of CO_2, N_2O, NO, and the formation of Cu_xO_x.

Key Reactions:

$$M_2(OH)_3NO_3 + SCPB \text{ (Hemicellulose)} \rightarrow CO_2 + N_2O + NO + M_xO_x$$

Step 3: Further Biomass Decomposition (280–450°C)

At higher temperatures, metal oxides (e.g., Cu_2O, Ni_2O_3) react with CO_2 and partial SCPB components (especially cellulose), producing CuO, NiO[71], CO, NO_2, HNO_3, and CH_4.

Key Reactions:

$$M_xO_x + SCPB \text{ (Cellulose)} \rightarrow CO_2 + CO + NO_2 + HNO_3 + CH_4 + MO + M$$

Step 4: Reduction of Metal Oxides and Biochar Formation (450–500°C, residence time 1h at 500°C)

At the highest temperatures, metal oxides (like CuO, NiO) are reduced to metallic copper, nickel and alloy, while biomass lignin decomposes, forming biochar. CO_2 is a key gaseous product formed during whole pyrolysis process.

Key Reactions:

MO + SCPB (Lignin) → M + SCPBB(biochar) + CO_2

MO + SCPBB (biochar) → M + SCPBB(porous biochar) + CO_2
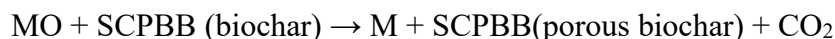
The metal oxides oxidize the biochar and contribute to the formation of the porous structure [72,73].

Since CO_2 is continuously produced over the whole pyrolysis temperature range, it is likely that this syngas contributes to forming the biochar porous structure. Indeed, pyrolysis under a CO_2 atmosphere yields a higher specific surface area than that conducted under nitrogen [74].

Conclusion

This study demonstrates that the pyrolysis of SCPB and SCPB/CuNi through wet impregnation leads to enhanced thermal conversion and the formation of biochar with distinct chemical and structural properties. The incorporation of metal nanoparticles, through wet impregnation and pyrolysis sequential steps, significantly reduces the activation energy (determined using FWO and DAEM methods), facilitating the thermochemical conversion process. FT-IR spectroscopy provided detailed insights into the gas phase products during the decomposition of hydrated copper and nickel nitrates on biomass. The analysis revealed stages of dehydration, nitrate decomposition, and reduction reactions, with corresponding gas phase products including water vapor, nitrogen dioxide, oxygen, carbon dioxide, and carbon monoxide. This method effectively monitored the transformations and provided a comprehensive understanding of the gas evolution in the thermal processing of nitrate salts on biomass. XPS and Raman analyses reveal that both TG-biochar (biochar obtained by TGA) and tubular furnace biochar share similar chemical compositions, including nitrogen-functionalized structures and graphitic carbon formation. This given strong supporting evidence that the actual study conducted by TG-FTIR accounts very well for the thermochemical conversion of SCPB biomass impregnated with copper and nickel nitrates, under similar pyrolysis conditions. Clearly, the TG-FTIR setup is a reliable technique to simulate the pyrolysis process in a tubular furnace which leads to reactive and

25

functional porous biochar loaded with metallic nanometals. Moreover, nickel could be regarded as an ideal activator (like the traditional $ZnCl_2$ and $FeCl_3$) for the pyrolysis of wet-impregnated biomass. It has multiple advantages: it activates pyrolysis and provides a biochar porous structure, it yields immobilized catalytic nanoparticles, and imparts magnetic properties to the biochar support.

Acknowledgements

References

[1] W. Colglazier, Sustainable development agenda: 2030, *Science, 349* (2015) 1048-1050. https://doi.org/10.1126/science.aad2333.

[2] M. Trane, L. Marelli, A. Siragusa, R. Pollo, P. Lombardi, Progress by Research to Achieve the Sustainable Development Goals in the EU: A Systematic Literature Review, *Sustainability, 15* (2023). https://doi.org/10.3390/su15097055.

[3] H. Hsu, E. Binyet, R.A.A. Nugroho, W.-C. Wang, P. Srinophakun, R.-Y. Chein, R. Demafelis, N. Chiarasumran, H. Saputro, A.F. Alhikami, N. Sakulshah, T. Laemthong, Toward sustainability of Waste-to-Energy: An overview, *Energy Convers. Manage., 321* (2024). https://doi.org/10.1016/j.enconman.2024.119063.

[4] Y. Song, J. Phipps, C. Zhu, S. Ma, Porous Materials for Water Purification, *Angewandte Chemie-International Edition, 62* (2023). https://doi.org/10.1002/anie.202216724.

[5] D. Aboagye, R. Djellabi, F. Medina, S. Contreras, Radical-Mediated Photocatalysis for Lignocellulosic Biomass Conversion into Value-Added Chemicals and Hydrogen: Facts, Opportunities and Challenges, *Angewandte Chemie-International Edition, 62* (2023). https://doi.org/10.1002/anie.202301909.

[6] J. Ufitikirezi, M. Filip, M. Ghorbani, T. Zoubek, P. Olsan, R. Bumbalek, M. Strob, P. Bartos, S.N. Umurungi, Y.T. Murindangabo, A. Hermanek, O. Tupy, Z. Havelka, R. Stehlik, P. Cerny, L. Smutny, Agricultural Waste Valorization: Exploring Environmentally Friendly Approaches to Bioenergy Conversion, *Sustainability, 16* (2024). https://doi.org/10.3390/su16093617.

[7] S. Pradhan, P. Parthasarathy, H.R. Mackey, T. Al-Ansari, G. McKay, Optimization of peapod peel biochar amendment for sustainable agriculture by surface response

methodology towards water-food-environment nexus, *Chem. Eng. J., 498* (2024). https://doi.org/10.1016/j.cej.2024.155243.

[8] C. Zhu, W. Wang, Z. Wu, X. Zhang, Z. Chu, Z. Yang, Preparation of cellulose-based porous adsorption materials derived from corn straw for wastewater purification, *Int. J. Biol. Macromol., 233* (2023). https://doi.org/10.1016/j.ijbiomac.2023.123595.

[9] M.A.M. Costa, N.C.B. Schiavon, M.P. Felizardo, A.J.D. Souza, K.J. Dussan, Emission analysis of sugarcane bagasse combustion in a burner pilot, *Sustainable Chemistry And Pharmacy, 32* (2023). https://doi.org/10.1016/j.scp.2023.101028.

[10] F. Ali, A. Dawood, A. Hussain, M.H. Alnasir, M.A. Khan, T.M. Butt, N.K. Janjua, A. Hamid, Fueling the future: biomass applications for green and sustainable energy, *Discover Sustainability, 5* (2024). https://doi.org/10.1007/s43621-024-00309-z.

[11] Y. Wang, S. Yang, G. Bao, H. Wang, Insight into nettle straw pyrolysis: Multicomponent kinetics, gas emissions and machine learning models, *J. Anal. Appl. Pyrolysis, 172* (2023). https://doi.org/10.1016/j.jaap.2023.106021.

[12] S. Huang, Y. Su, W. Luo, Q. He, S. Huang, N. Zhou, Z. Zhou, Kinetic analysis and in-situ no support catalytic pyrolysis product distribution of Chinese herb residue, *J. Anal. Appl. Pyrolysis, 156* (2021). https://doi.org/10.1016/j.jaap.2021.105114.

[13] Z. Sun, H. Wang, Y. Zeng, J. Liu, N. Maeda, Understanding and enhancing the phase stability of fast pyrolysis oils through ternary phase diagrams, *Chem. Eng. J., 500* (2024). https://doi.org/10.1016/j.cej.2024.156820.

[14] K. Zhang, R. Cen, H. Moavia, Y. Shen, A. Ebihara, G. Wang, T. Yang, R. Sakrabani, K. Singh, Y. Feng, F. Lian, C. Ma, B. Xing, The role of biochar nanomaterials in the application for environmental remediation and pollution control, *Chem. Eng. J., 492* (2024). https://doi.org/10.1016/j.cej.2024.152310.

[15] A. Kalla, N. Mayilswamy, B. Kandasubramanian, P. Mahajan-Tatpate, Biochar: a sustainable and an eco-friendly material for energy storage applications, *International Journal Of Green Energy, 21* (2024) 1695-1709. https://doi.org/10.1080/15435075.2023.2259973.

[16] M.Z. Yameen, S.R. Naqvi, D. Juchelkova, M.N.A. Khan, Harnessing the power of functionalized biochar: progress, challenges, and future perspectives in energy, water treatment, and environmental sustainability, *Biochar, 6* (2024). https://doi.org/10.1007/s42773-024-00316-3.

[17] X. Yuan, Y. Shen, P.A. Withana, O. Masek, C.S.K. Lin, S. You, F.M.G. Tack, Y.S. Ok, Thermochemical upcycling of food waste into engineered biochar for energy and environmental applications: A critical review, *Chem. Eng. J., 469* (2023). https://doi.org/10.1016/j.cej.2023.143783.

[18] T. Khandaker, T. Islam, A. Nandi, M.A.A.M. Anik, M.S. Hossain, M.K. Hasan, M.S. Hossain, Biomass-derived carbon materials for sustainable energy applications: a comprehensive review, *Sustainable Energy & Fuels,* (2024). https://doi.org/10.1039/d4se01393j.

[19] A. Gamal, K. Jlassi, Y.H. Ahmad, M. Tang, S.Y. Al-Qaradawi, M.M. Chehimi, K.I. Ozoemena, A.M. Abdullah, Carbon-supported catalysts for carbon dioxide methanation: A review, *Journal Of Co2 Utilization, 85* (2024). https://doi.org/10.1016/j.jcou.2024.102881.

[20] Z. Lou, Y. Zhang, Y. Li, L. Xu, Study on microscopic physical and chemical properties of biomass materials by AFM, *Journal Of Materials Research And Technology-Jmr&T, 24* (2023) 10005-10026. https://doi.org/10.1016/j.jmrt.2023.05.176.

[21] J. Cai, N. Lin, Y. Li, J. Xue, F. Li, L. Wei, M. Yu, X. Zha, W. Li, Research on the application of catalytic materials in biomass pyrolysis, *J. Anal. Appl. Pyrolysis, 177* (2024). https://doi.org/10.1016/j.jaap.2023.106321.

[22] Y. Mahmoud Elsafi, Beh Hoe Guan, Wai Hong Leong, Norhana Mohamed Rashid Catalytic potential of biochar: enhancing pollution removal through persistent free radicals in biomass pyrolysis — a review, *Biomass Convers. Biorefin.,* (2025). https://doi.org/10.1007/s13399-024-06441-0.

[23] Y. Huang, Q. Wu, J. Yan, F. Chu, Y. Xu, D. Li, H. Zhang, S. Yang, Efficient removal and recovery of phosphate by biochar loaded with ultrafine MgO nanoparticles, *Environ. Res., 266* (2025). https://doi.org/10.1016/j.envres.2024.120518.

[24] D. Wang, H. Wang, Z. Tan, A.S.A. Almalki, A.M. Fallatah, S. Yang, Z. Shi, In-situ preparation of $CuO/Cu_2O/Cu/N$-codoped biochar from chitosan derivative: Adsorption property and photo-Fenton catalytic performance in removal of antibiotic, *Advanced Composites And Hybrid Materials, 8* (2025). https://doi.org/10.1007/s42114-024-01069-0.

[25] X. Liao, H. Cui, H. Luo, Y. Lv, P. Liu, Highly efficient selective hydrodeoxygenation of 5-hydroxymethylfurfural to 2,5-dimethylfuran over Co-Ni-situ encapsulated in biochar-based carbon catalysts: The crucial role of CoNi alloys and Co-Nx species, *Chem. Eng. J., 503* (2025). https://doi.org/10.1016/j.cej.2024.158336.

[26] H. Lyu, X. Wang, P. Li, P. Yan, J. Tang, Mn/Co bimetallic catalyst immobilized on N-doped biochar for enhanced photocatalytic degradation of sulfanilamide in water, *Applied Catalysis B-Environment And Energy, 354* (2024). https://doi.org/10.1016/j.apcatb.2024.124123.

[27] J. Luo, K. Sun, S. Sun, R. Ma, C. Cui, H. Cui, Mg and Fe co-loaded biochar prepared by microwave-synergized K2FeO4 of marine biomass for efficient CO2 capture: Performance assessment and mechanism exploration, *Chem. Eng. J., 500* (2024). https://doi.org/10.1016/j.cej.2024.157102.

[28] D. Castilla-Caballero, A. Hernandez-Ramirez, S. Vazquez-Rodriguez, J. Colina-Marquez, F. Machuca-Martinez, J. Barraza-Burgos, A. Roa-Espinosa, A. Medina-Guerrero, S. Gunasekaran, Effect of pyrolysis, impregnation, and calcination conditions on the physicochemical properties of TiO_2/Biochar composites intended for photocatalytic applications, *Journal Of Environmental Chemical Engineering, 11* (2023). https://doi.org/10.1016/j.jece.2023.110274.

[29] J. Gopalan, A. Buthiyappan, A.A.A. Raman, Insight into metal-impregnated biomass based activated carbon for enhanced carbon dioxide adsorption: A review, *Journal Of Industrial And Engineering Chemistry, 113* (2022) 72-95. https://doi.org/10.1016/j.jiec.2022.06.026.

[30] M. Geca, A.M. Khalil, M.Q. Tang, A.K. Bhakta, Y. Snoussi, P. Nowicki, M. Wisniewska, M.M. Chehimi, Surface Treatment of Biochar-Methods, Surface Analysis

and Potential Applications: A Comprehensive Review, *Surfaces, 6* (2023) 179-213. https://doi.org/10.3390/surfaces6020013.

[31] Y. Zhang, Y. Liang, S. Li, Y. Yuan, D. Zhang, Y. Wu, H. Xie, K. Brindhadevi, A. Pugazhendhi, C. Xia, A review of biomass pyrolysis gas: Forming mechanisms, influencing parameters, and product application upgrades, *Fuel, 347* (2023). https://doi.org/10.1016/j.fuel.2023.128461.

[32] D. Sangare, M. Moscosa-Santillan, S. Bostyn, V. Belandria, A.D.l.C. Martinez, L. Van De Steene, Multi-step kinetic mechanism coupled with CFD modeling of slow pyrolysis of biomass at different heating rates, *Chem. Eng. J., 479* (2024). https://doi.org/10.1016/j.cej.2023.147791.

[33] A.T. Kocer, B. Karacaoglu, G.A. Karaca, B. Inan, D. Balkanli, Thermal behavior analysis and biochar formation through co-pyrolysis of de-oiled microalgae biomass and wood sawdust for ecofriendly resource utilization, *Algal Research-Biomass Biofuels And Bioproducts, 82* (2024). https://doi.org/10.1016/j.algal.2024.103674.

[34] H. Mo, X. Chen, T. Mo, C. Wu, W. Wei, Y. Wu, Q. Li, J. Liang, L. Wang, Optimization model for co-pyrolytic synergy: A case study in starch sludge with chicken manure and comprehensive investigation combining kinetics, bio-products characterization, and DFT-based decomposition pathways, *Fuel, 380* (2025). https://doi.org/10.1016/j.fuel.2024.133138.

[35] A. Asghar, C. Liu, I. Ali, A.Z. Khan, H. Zhu, N. Wang, M. Nawaz, T.A. Tabish, M.A. Mehmood, R.T. Rasool, Bioenergy potential of Saccharum bengalense through pyrolysis, reaction kinetics, TG-FTIR-GCMS analysis of pyrolysis products, and validation of the pyrolysis data through machine learning, *Chem. Eng. J., 465* (2023). https://doi.org/10.1016/j.cej.2023.142930.

[36] V. Piazza, R.B.d.S. Junior, A. Frassoldati, L. Lietti, S. Chiaberge, C. Gambaro, A. Siviero, T. Faravelli, A. Beretta, Detailed speciation of biomass pyrolysis products with a novel TGA-based methodology: the case-study of cellulose, *J. Anal. Appl. Pyrolysis, 178* (2024). https://doi.org/10.1016/j.jaap.2024.106413.

[37] M. Tang, Y. Snoussi, A.K. Bhakta, M. El Garah, A.M. Khalil, S. Ammar, M.M. Chehimi, Unusual, hierarchically structured composite of sugarcane pulp bagasse biochar loaded with Cu/Ni bimetallic nanoparticles for dye removal, *Environ. Res., 232* (2023) 116232-116232. https://doi.org/10.1016/j.envres.2023.116232.

[38] M. Tang, A.K. Bhakta, Y. Snoussi, K. Jlassi, M. El Garah, M.M. Chehimi, Pyrolysis temperature effect on the efficacy of biochar/CuNi composite catalysts for emerging pollutant degradation, *Surf. Interfaces, 50* (2024). https://doi.org/10.1016/j.surfin.2024.104446.

[39] J. Liu, X. Yang, H. Liu, X. Jia, Y. Bao, Mixed biochar obtained by the co-pyrolysis of shrimp shell with corn straw: Co-pyrolysis characteristics and its adsorption capability, *Chemosphere, 282* (2021). https://doi.org/10.1016/j.chemosphere.2021.131116.

[40] T.N. Rafenomananjara, S. Kudo, J. Sperry, S. Asano, J.-i. Hayashi, Phytic acid as a biorenewable catalyst for cellulose pyrolysis to produce levoglucosenone, *Rsc Sustainability,* (2024). https://doi.org/10.1039/d4su00502c.

[41] A.K.B. Mengqi Tang, Youssef Snoussi, Khouloud Jlassi, Mohamed El Garah, Mohamed M. Chehimi Pyrolysis temperature effect on the efficacy of biochar/CuNi composite catalysts for emerging pollutant degradation, *Surf. Interfaces, 50* (2024). https://doi.org/10.1016/j.surfin.2024.104446.

[42] Y.M. Faleeva, V.A. Lavrenov, V.M. Zaichenko, Investigation of plant biomass two-stage pyrolysis based on three major components: cellulose, hemicellulose, and lignin, *Biomass Convers. Biorefin., 14* (2024) 14519-14529. https://doi.org/10.1007/s13399-022-03385-1.

[43] A. Ashok, A. Kumar, R.R. Bhosale, M.A.H. Saleh, L.J.P. van den Broeke, Cellulose assisted combustion synthesis of porous Cu-Ni nanopowders, *Rsc Advances, 5* (2015) 28703-28712. https://doi.org/10.1039/c5ra03103f.

[44] F. Pahlavan, H. Kaur, L.K.G. Ackerman-Biegasiewicz, A. Lamanna, E.H. Fini, Application of algal biochar to prevent leachate of heavy metals from mine tailings, *Resources Conservation And Recycling, 210* (2024). https://doi.org/10.1016/j.resconrec.2024.107810.

[45] E. Torres-Garcia, L.F. Ramirez-Verduzco, J. Aburto, Pyrolytic degradation of peanut shell: Activation energy dependence on the conversion, *Waste Manage. (Oxford), 106* (2020) 203-212. https://doi.org/10.1016/j.wasman.2020.03.021.

[46] C. Sun, C. Li, H. Tan, Y. Zhang, Synergistic effects of wood fiber and polylactic acid during co-pyrolysis using TG-FTIR-MS and Py-GC/MS, *Energy Convers. Manage., 202* (2019). https://doi.org/10.1016/j.enconman.2019.112212.

[47] K. Kucerova, Z. Machala, K. Hensel, Transient Spark Discharge Generated in Various N_2O_2 Gas Mixtures: Reactive Species in the Gas and Water and Their Antibacterial Effects, *Plasma Chem. Plasma Process., 40* (2020) 749-773. https://doi.org/10.1007/s11090-020-10082-2.

[48] D. Trunec, Z. Navratil, J. Tomekova, V. Mazankova, S. Durcanyova, A. Zahoranova, Chemical composition of gaseous products generated by coplanar barrier discharge in air and N_2O_2 mixtures, *Plasma Sources Science & Technology, 31* (2022). https://doi.org/10.1088/1361-6595/ac9c8f.

[49] E.A. Varol, U. Mutlu, TGA-FTIR Analysis of Biomass Samples Based on the Thermal Decomposition Behavior of Hemicellulose, Cellulose, and Lignin, *Energies, 16* (2023). https://doi.org/10.3390/en16093674.

[50] M. Ishfaq, A. Asghar, I. Ali, A.Z. Khan, A. Shahid, N. Wang, H. Zhu, H.R. El-Seedi, M.A. Mehmood, C.-G. Liu, Appraisal of wastewater-grown biomass of Leptochloa fusca to produce bioenergy and biochemicals through pyrolysis, TG-FTIR-GCMS, and machine learning tools, *Energy Convers. Manage., 304* (2024). https://doi.org/10.1016/j.enconman.2024.118229.

[51] X. Zhang, Y. Li, X. Zhang, P. Ma, X. Xing, Co-combustion of municipal solid waste and hydrochars under non-isothermal conditions: Thermal behaviors, gaseous emissions and kinetic analyses by TGA-FTIR, *Energy, 265* (2023). https://doi.org/10.1016/j.energy.2022.126373.

[52] X.-F. Zhou, W.-Q. Geng, X.-Y. Ma, C.-F. Ran, K. Liu, Dynamics of NO, N_2O, and ONOOH in atmospheric-pressure air dielectric barrier discharge: decoupling energy

density and gas temperature effects varying with discharge voltage, *Journal Of Physics D-Applied Physics, 57* (2024). https://doi.org/10.1088/1361-6463/ad2bdc.

[53] F. Delachaux, C. Vallieres, H. Monnier, M.T. Lecler, Experimental study of NO and NO_2 adsorption on a fresh or dried NaY zeolite: influence of the gas composition by breakthrough curves measurements, *Adsorption-Journal Of the International Adsorption Society, 25* (2019) 95-103. https://doi.org/10.1007/s10450-018-9989-3.

[54] A. Soria-Verdugo, M.T. Morgano, H. Maetzing, E. Goos, H. Leibold, D. Merz, U. Riedel, D. Stapf, Comparison of wood pyrolysis kinetic data derived from thermogravimetric experiments by model-fitting and model-free methods, *Energy Convers. Manage., 212* (2020). https://doi.org/10.1016/j.enconman.2020.112818.

[55] P. Gimenez, S. Fereres In *Effect of heating rates and composition on the thermal decomposition of nitrate based molten salts*, International Conference on Concentrating Solar Power and Chemical Energy Systems (SolarPACES), Beijing, PEOPLES R CHINA, Sep 16-19; Beijing, PEOPLES R CHINA, **2015**; pp 654-662.

[56] S. Belbekhouche, S.I. Kebe, S. Mahouche-Chergui, M. Guerrouache, B. Carbonnier, M. Jaziri, M.M. Chehimi, Aryl diazonium-modified olive waste: A low cost support for the immobilization of nanocatalysts, *Colloids And Surfaces a-Physicochemical And Engineering Aspects, 529* (2017) 541-549. https://doi.org/10.1016/j.colsurfa.2017.06.011.

[57] N. Xu, J.H. Bhadha, A. Rabbany, S. Swanson, J.M. McCray, Y.C. Li, S.L. Strauss, R. Mylavarapu, Crop Nutrition and Yield Response of Bagasse Application on Sugarcane Grown on a Mineral Soil, *Agronomy-Basel, 11* (2021). https://doi.org/10.3390/agronomy11081526.

[58] A.M. Khalil, L. Michely, R. Pires, S. Bastide, K. Jlassi, S. Ammar, M. Jaziri, M.M. Chehimi, Copper/Nickel-Decorated Olive Pit Biochar: One Pot Solid State Synthesis for Environmental Remediation, *Applied Sciences-Basel, 11* (2021). https://doi.org/10.3390/app11188513.

[59] U.P. Agarwal, Analysis of Cellulose and Lignocellulose Materials by Raman Spectroscopy: A Review of the Current Status, *Molecules, 24* (2019). https://doi.org/10.3390/molecules24091659.

[60] K.L. Larsen, S. Barsberg, Theoretical and Raman Spectroscopic Studies of Phenolic Lignin Model Monomers, *J. Phys. Chem. B, 114* (2010) 8009-8021. https://doi.org/10.1021/jp1028239.

[61] T.K. N Gierlinger, M Harrington, Manfred Schwanninger, Raman imaging of lignocellulosic feedstock. In *Cellulose biomass conversion*, T. V. de Ven, J. K., Ed. 2013.

[62] L. Chavez-Guerrero, S. Vazquez-Rodriguez, J.A. Salinas-Montelongo, L.E. Roman-Quirino, N.A. Garcia-Gomez, Preparation of all-cellulose composites with optical transparency using the banana pseudostem as a raw material, *Cellulose, 26* (2019) 3777-3786. https://doi.org/10.1007/s10570-019-02369-1.

[63] C.T.K. Tran, H.T.T. Tran, H.T.T. Bui, T.Q. Dang, L.Q. Nguyen, Determination of low level nitrate/nitrite contamination using SERS-active Ag/ITO substrates coupled to a self-designed Raman spectroscopy system, *Journal Of Science-Advanced Materials And Devices, 2* (2017) 172-177. https://doi.org/10.1016/j.jsamd.2017.05.002.

[64] M.D.F.K.B.M.T.H. Kauffmann, Raman spectroscopic sensors for inorganic salts. In *Spectroscopic Properties of Inorganic and Organometallic Compounds: Techniques, Materials and Applications*, Duckett, J. Y. R. D. S., Ed. 2023; Vol. 44, pp 40 - 67.

[65] R. Liaqat, M.A. Mansoor, J. Iqbal, A. Jilani, S. Shakir, A. Kalam, S. Wageh, Fabrication of Metal (Cu and Cr) Incorporated Nickel Oxide Films for Electrochemical Oxidation of Methanol, *Crystals, 11* (2021). https://doi.org/10.3390/cryst11111398.

[66] S. Vivek, S. Preethi, A.K. Sundramoorthy, K.S. Babu, The composition dependent structure and catalytic activity of nanostructured Cu-Ni bimetallic oxides, *New J. Chem., 44* (2020) 9691-9698. https://doi.org/10.1039/d0nj01753a.

[67] S.G.C. de Almeida, L.A.C. Tarelho, T. Hauschild, M.A.M. Costa, K.J. Dussan, Biochar production from sugarcane biomass using slow pyrolysis: Characterization of the solid fraction, *Chemical Engineering And Processing-Process Intensification, 179* (2022). https://doi.org/10.1016/j.cep.2022.109054.

[68] M. Tang, Y. Snoussi, A.K. Bhakta, M. El Garah, A.M. Khalil, S. Ammar, M.M. Chehimi, Unusual, hierarchically structured composite of sugarcane pulp bagasse biochar loaded with Cu/Ni bimetallic nanoparticles for dye removal, *Environ. Res., 232* (2023). https://doi.org/10.1016/j.envres.2023.116232.

[69] I.V. Morozov, K.O. Znamenkov, Y.M. Korenev, O.A. Shlyakhtin, Thermal decomposition of $Cu(NO_3)_2 \cdot 3H_2O$ at reduced pressures, *Thermochim. Acta, 403* (2003) 173-179. https://doi.org/10.1016/s0040-6031(03)00057-1.

[70] A. Kumar, E.E. Wolf, A.S. Mukasyan, Solution Combustion Synthesis of Metal Nanopowders: Copper and Copper/Nickel Alloys, *AlChE J., 57* (2011) 3473-3479. https://doi.org/10.1002/aic.12537.

[71] H. Bayoka, Y. Snoussi, A.K. Bhakta, M. El Garah, A.M. Khalil, M. Jouini, S. Ammar, M.M. Chehimi, Evidencing the synergistic effects of carbonization temperature, surface composition and structural properties on the catalytic activity of biochar/ bimetallic composite, *J. Anal. Appl. Pyrolysis, 173* (2023). https://doi.org/10.1016/j.jaap.2023.106069.

[72] D. Li, L. Zhao, X. Cao, Z. Xiao, H. Nan, H. Qiu, Nickel-catalyzed formation of mesoporous carbon structure promoted capacitive performance of exhausted biochar, *Chem. Eng. J., 406* (2021). https://doi.org/10.1016/j.cej.2020.126856.

[73] X. Tian, Y. Wang, Z. Zeng, L. Dai, J. Xu, K. Cobb, L. Ke, R. Zou, Y. Liu, R. Ruan, Research progress on the role of common metal catalysts in biomass pyrolysis: a state-of-the-art review, *Green Chem., 24* (2022) 3922-3942. https://doi.org/10.1039/d1gc04537g.

[74] Z. Yi, C. Li, L. Zhang, S. Zhang, W. Gao, S. Wang, B. Li, X. Hu, Impacts of CO_2 atmosphere on property of the biochar from pyrolysis of lignin, *J. Anal. Appl. Pyrolysis, 167* (2022). https://doi.org/10.1016/j.jaap.2022.105689.